CEAS-GNC-2022-057

CEAS EuroGNC 2022
"Conference on Guidance, Navigation and Control"
3-5 May 2022 @ Technische Universität Berlin, Germany

Examination of the Dynamic Modes of a Single-Seater Fighter Jet During Aerial Refuelling

Luke H. Peristy Doctoral Candidate, Royal Military College of Canada, Department of Mechanical and Aerospace Engineering, Kingston, Ontario, Canada, K7K 7B4. luke.peristy@rmc.ca

Ruben E. Perez Associate Professor, Royal Military College of Canada, Department of Mechanical and Aerospace Engineering, Kingston, Ontario, Canada, K7K 7B4. ruben.perez@rmc.ca

ABSTRACT

This paper presents a multi-modal analysis framework which is used to examine the interactions between a C-130 tanker aircraft and F/A-18 refueller during AAR for the purposes of predicting handling qualities during the AAR task. This work is motivated by the need to rapidly clear tanker-refueller pairs for safe operation in the event of multilateral operation between groups with different refuelling platforms. The framework uses a vortex panel method with an actuator disk propulsion model to predict air velocities in the tanker wake. A vortex panel representation of the refueller is then combined with a closed-form aerodynamic model to find the trim points at various locations in the tanker's wake. The positional stability of the refueller is examined, finding areas of positional stability within the bounds of the tanker's wingspan. A simplified controller model is combined with 6-DOF, 9-state equations to predict the closed-loop natural modes at the trim points within the tanker wake. The closed-loop eigenvalues of the 9-state system are not predicted to change appreciably during refuelling compared to steady level flight. However, examination of the eigenvectors shows cross-coupling effects. Due to this cross-coupling, it is theorized that a purely eigenvalue based analysis will be insufficient to predict handling qualities during AAR. Therefore, it is suggested that frequency and bandwidth-based handling quality assessment criteria be examined.

Nomenclature

α	=	Angle of attack (rad)
β	=	Sideslip angle (rad)
$(\delta_{\text{ail}}\ \delta_{\text{ele}}\ \delta_{\text{rud}})$	=	Aileron deflection, elevator deflection, rudder deflection (rad)
Γ	=	Vortex ring strength
ρ	=	Density of air (kg/m^3)
$(\phi,\ \theta,\ \psi)$	=	Roll angle, pitch angle, yaw angle (rad)
$a_{\square\square}$	=	Aerodynamic influence coefficient
AIC	=	Aerodynamic influence coefficient matrix
b	=	Wingspan (m)
$\bar{c}$	=	Mean aerodynamic chord (m)

$(C_L, C_D, \text{and } C_Y)$	=	Coefficient of lift, drag, and sideforce
$(C_l, C_m, \text{and } C_n)$	=	Coefficient of roll, pitch, and yaw
g	=	Gravitational acceleration, 9.81 $\mathrm{m/s^2}$
I_{xx}	=	Moment of Inertia about x ($\mathrm{kg \cdot m^2}$)
I_{xz}	=	Cross Product of Inertia about y ($\mathrm{kg \cdot m^2}$)
I_{yy}	=	Moment of Inertia about y ($\mathrm{kg \cdot m^2}$)
I_{zz}	=	Moment of Inertia about z ($\mathrm{kg \cdot m^2}$)
M_∞	=	Mach number
M_α	=	Derivative of pitching moment with respect to angle of attack (N·m/rad)
M_q	=	Derivative of pitching moment with respect pitch rate (N·m·s/rad)
m	=	Mass (kg)
n	=	Normal vector
$\bar{q}$	=	Dynamic pressure = $\frac{1}{2}\rho V^2$ (Pa)
R	=	Propeller radius (m)
r	=	Radial coordinate (m)
RHS	=	Boundary condition right-hand-side vector
S	=	Wing area ($\mathrm{m^2}$)
T	=	Thrust (N)
$_t$	=	Indicates tanker
(p, q, r)	=	Roll, pitch, and yaw rates (rad/s)
$_r$	=	Indicates refueller
(u, v, w)	=	x, y, and z components of velocity (m/s)
U_{inf}	=	Freestream velocity vector (m/s)
U_{wake}	=	Wake velocity vector (m/s)
V_x	=	Axial velocity (m/s)
V_r	=	Radial velocity (m/s)
V	=	Aircraft velocity state (m/s)
Z_α	=	Derivative of body force in the Z direction with respect to angle of attack, (N/rad)

1 Introduction

This work is motivated by understanding and predicting pilot workload and handling qualities for an air-to-air refuelling (AAR) task, specifically during probe-and-drogue refuelling (PDR). Clearing tanker-receiver pairs for operation involves a combination of analysis and flight testing[1] which is intended to predict the effect of the tanker wake on the refuelling aircraft in order to determine if the refuelling procedure can be completed safely. However, the need to rapidly clear tanker-refueller pairs for safe operation in the event of multilateral operation between groups with different refuelling platforms necessitates analysis methods which do not involve flight testing. AAR analysis is also of interest for unmanned aerial vehicle (UAV) control system design, with linear, non-linear, and adaptive control strategies being examined to optimize for both stability and robustness[2]. Advancements in AAR in the past 20 years have been predominantly driven by the continuing development of unmanned aerial systems (UAS) which must demonstrate a human level of proficiency in their ability to perform AAR procedures as a requirement of airworthiness certification [3].

Most early work in AAR modelling focused on predicting the air velocities in the tanker wake, with Bloy et al; Blake et al; and Dogan et al. concentrating their efforts on the use of potential flow methods, such as horseshoe vortices[4, 5], vortex lattice methods[6, 7], and medium-fidelity methods such as Euler simulations[8] and Vortex Effect Modelling Techniques (VEMTs)[9]. Use of these medium-fidelity methods is desirable due to the rapidity with which results can be generated. Although an increase in fidelity can produce better predictions of viscous effects, VLMs have demonstrated an ability to capture major effects in terms of pitch, roll, and yaw on an aircraft which is flying in the wake of another aircraft. Additionally, a CFD analysis requires comparatively more time and computational resources to generate its high fidelity results compared to a low/medium fidelity analysis[2, 10]. Typically, CFD analyses are only used for specific combinations of tanker and refuelling aircraft[10]. Furthermore, the amount of data generated by CFD analyses can be prohibitive in terms of memory usage in simulations. Fezans and Jann have stated that the data imported into a real time simulation requires a compromise between precision and memory usage[11].

While much of the previous work has concentrated on modelling, simulation, and experimentation, there appears to have been little work done to predict pilot workload during AAR. Flying qualities estimation and evaluation has been tackled from a simulation perspective by Lu et al[12]. In this work, a human-in-the-loop flight simulation was used to evaluate handling qualities for a probe and drogue refuelling task for a variety of different controller gains. They suggest a longitudinal handling-quality metric based on the pitch axis gain and the transfer function between the rate feedback and command input. This present work examines dynamic modes of an F/A-18 flying in the wake of a C-130 Hercules during a refuelling procedure and make predictions about the pilot workload and flying qualities based on MIL-HDBK-1797 and MIL-F-8785C. Previous work by Peristy et al.[13] attempted to predict handling qualities based on a coupled vortex panel analysis, and longitudinal and lateral-directional dynamic mode approximations. Building on this work, the present paper makes improvements to the previous method by accounting for propulsive effects of the tanker, adds the use of a closed-form aerodynamic model to determine aerodynamic stiffness and damping quantities, uses a nine-state model to predict flight dynamics instead of a simplified approximation, and adds a simple controller model for closed-loop mode analysis.

2 Methodology

The methodology used combines a variety of methods including a closed-form aerodynamic model to predict aircraft dynamics, a vortex panel method, and actuator disk model to predict the air velocities in

the tanker wake and evaluate their effect on an aircraft flying in the wake. Figure 1 shows the relationship between the various methodologies and the analysis objectives which they are used to accomplish.

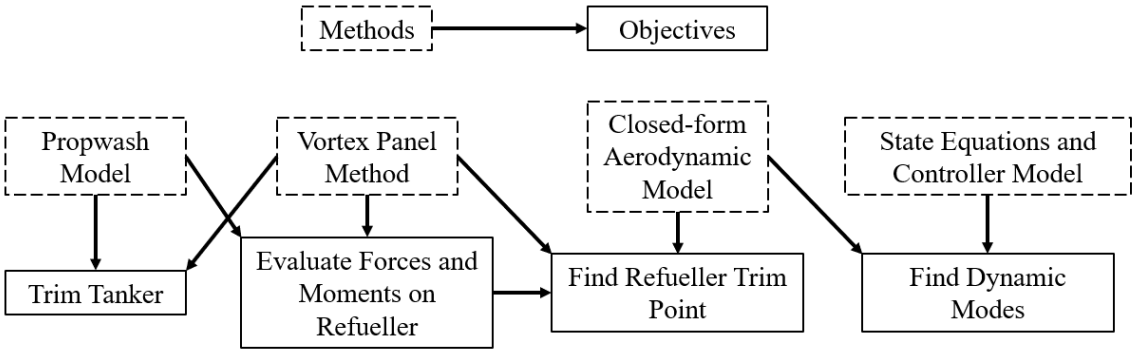

Fig. 1 Schematic showing the relationship between framework objectives and methodology used.

The analysis is performed in a three-step process. First the tanker's trim point is found, then the forces and moments on the refueller are found in order to find the refueller trim point. After the refueller trim point is found, the dynamic modes can be calculated.

2.1 Vortex Panel Method

The vortex panel method used is detailed in Katz and Plotkin[14], and models aircraft and lifting surfaces by solving for a set of vortex ring strengths (Γ) which are proportional to the lift generated by each panel using a set of linear equations described by an aerodynamic influence coefficient (AIC) matrix, and boundary conditions given by the freestream velocity vector (U_∞) and the set of normal vectors at surface collocation points n.

The aerodynamic influence of panel n on the collocation point of panel m is given by the dot product

$$a_{mn} = (u, v, w)_{mn} \cdot n_m \tag{1}$$

where (u, v, w) is the velocity induced by vortex ring n. The AIC is populated by influence coefficients of each vortex ring at each collocation point. The influence of each ring vortex on each collocation point must be added. At some collocation point m, the total influence from all K vortex rings must be such that

$$\sum_{s=1}^{K} = a_{ms}\Gamma_s = -U_\infty \cdot n_m \tag{2}$$

which is to say that the velocity induced by every vortex panel at each collocation point must be equal and opposite to the freestream velocity component which is parallel to the panel's normal vector. A full vortex panel system with K vortex rings and collocation points can be represented in matrix form as follows:

$$\begin{bmatrix} a_{11} & a_{12} & a_{13} & \dots & a_{1K} \\ a_{21} & a_{22} & a_{23} & \dots & a_{2K} \\ \vdots & \vdots & \vdots & \ddots & \vdots \\ a_{K1} & a_{K2} & a_{K3} & \dots & a_{KK} \end{bmatrix} \begin{Bmatrix} \Gamma_1 \\ \Gamma_2 \\ \vdots \\ \Gamma_K \end{Bmatrix} = \begin{Bmatrix} -U_\infty \cdot n_1 \\ -U_\infty \cdot n_2 \\ \vdots \\ -U_\infty \cdot n_K \end{Bmatrix} \tag{3}$$

By denoting the vector on the right hand side of the equation as RHS, Equation 3 can be represented as

$$\text{AIC}\,\Gamma = RHS \tag{4}$$

For a simple vortex lattice system, Γ is found by inverting the AIC matrix. By adjusting the direction of the normal vectors of the tanker vortex panel system, a solution of vortex ring strengths can be found such that the total lift generated is equal to the presumed weight of the aircraft which the vortex panel system is representing. These vortex ring strengths can then be used to predict air velocities in the wake of the aircraft. These velocities at each collocation point are then added to the freestream velocity vector in the RHS of the refueller vortex panel method equation as follows:

$$\begin{bmatrix} a_{11} & a_{12} & a_{13} & \dots & a_{1K} \\ a_{21} & a_{22} & a_{23} & \dots & a_{2K} \\ \vdots & \vdots & \vdots & \ddots & \vdots \\ a_{K1} & a_{K2} & a_{K3} & \dots & a_{KK} \end{bmatrix} \begin{Bmatrix} \Gamma_1 \\ \Gamma_2 \\ \vdots \\ \Gamma_K \end{Bmatrix} = \begin{Bmatrix} -(U_\infty + U_{\text{wake}}) \cdot n_1 \\ -(U_\infty + U_{\text{wake}}) \cdot n_2 \\ \vdots \\ -(U_\infty + U_{\text{wake}}) \cdot n_K \end{Bmatrix} \tag{5}$$

Flow induced by propwash is also included in the U_{wake} term.

2.2 Propwash Model

Propulsion effects from propwash are accounted for using the closed-form actuator disk model first demonstrated by Conway[15] and its use has been demonstrated in various panel codes including those of Droandi *et al.*[16] and Alba *et al.*[17] The flowfield induced by the actuator disk is defined by the following set of equations for $V_x(r,x)$, the velocity in the streamwise direction, and $V_r(r,x)$, the velocity in the radial direction. In this formulation, R is the propeller radius, r is a radial coordinate which is 0 along the slipstream axis, and x is the axial coordinate.

$$V_x(r,0) = \frac{V_{x_0}}{R}\sqrt{R^2 - r^2} \tag{6}$$

$$V_x(r,x) = 2V_x(r,0) + V_{x_0}\left(-a + \frac{x}{R}\arcsin\left[\frac{2R}{\sqrt{x^2+(R+r)^2}+\sqrt{x^2+(R^2-r^2)}}\right]\right) \tag{7}$$

$$V_r(r,x) = \frac{V_{x_0}|x|}{2r}\left(\frac{1}{a} - a\right) - \frac{V_{x_0} r}{2R}\arcsin\left[\frac{2R}{\sqrt{x^2+(R+r)^2}+\sqrt{x^2+(R^2-r^2)}}\right] \tag{8}$$

$$a = \sqrt{\frac{\sqrt{(R^2-r^2-x^2)^2 + 4R^2x^2} + R^2 - r^2 - x^2}{2R^2}} \tag{9}$$

2.3 Aerodynamic Model

The aerodynamic model used in this work is based on the F/A-18 aerodynamic model published by Chakraborty[18] and which itself is based on flight test data published by Napolitano and Spagunolo[19] and Iliff and Wang[20]. The model defines the aircraft's moment and force coefficients as closed-form expressions that are non-linear functions of α, β, control surface deflections, and kinematic rates. This model can be easily adapted to different aircraft, as different model coefficients can be found by fitting the model to different aerodynamic data. Note that some quantities, such as the lift force, lift coefficient

C_L, and the pitch stiffness $\frac{\partial C_m}{\partial \alpha}$ are calculated using the vortex panel method in this section. The closed form equations which define the aerodynamic model used are given in the Appendix.

2.4 Trim Equations

Both tanker and refueller are assumed to be in steady level flight. For the tanker, that requires:

$$L_t = W_t \qquad \text{and} \qquad m_t = 0 \tag{10}$$

where L_t is a function of the tanker's angle of attack α_t and m_t is a function of α_t and the tanker's elevator deflection δ_{e_t}. By flying in the wake of the tanker, the refuelling aircraft is subject to various aerodynamic forces and moments that must be counteracted by flying with a certain flight path angle, bank angle, thrust and control surface deflections. Additionally, it should be noted that by flying within the downwash of the tanker wake, the aircraft will be subject to an "effective" angle of attack and sideslip angle which differ from the body rotation angles θ and ψ. The trim equations for the refueller are therefore:

$$L_r(\theta,\phi) + T\sin[\theta] = W_r \tag{11}$$

$$D_r(\alpha_{\text{eff}}) + T\cos[\theta] = 0 \tag{12}$$

$$Y_r(\phi, \delta_{\text{ail}}, \delta_{\text{rud}}) = 0 \tag{13}$$

$$m_r(\alpha_{\text{eff}}, \delta_{\text{ele}}) = 0 \tag{14}$$

$$l_{\text{ind}} + l_r(\alpha_{\text{eff}}, \delta_{\text{ail}}, \delta_{\text{rud}}) = 0 \tag{15}$$

$$n_r(\alpha_{\text{eff}}, \beta_{\text{eff}}, \delta_{\text{ele}}) = 0 \tag{16}$$

A simplifying assumption made in the above is that the rolling moment induced in the wake is due to the velocity gradient across the lifting surfaces, whereas the yawing moment is caused by the effective sideslip angle β_{eff}. As the effective angle of attack is equal to the flight path angle plus the angle induced by the downwash, $\alpha_{\text{eff}} = \theta + \Delta_{\text{ind}}$, the above series of six equations has six unknowns: $\theta, \phi, T, \delta_{\text{ail}}, \delta_{\text{ele}}, \delta_{\text{rud}}$.

2.5 State Equations

The equations of motion are a six-DOF, nine-state mathematical model are derived in NASA Contractor Report 194838[19] and presented here. The equations of motion take the form

$$\dot{x} = f(x,u) \tag{17}$$

where $x := [V\ (\text{m/s}), \beta\ (\text{rad}), \alpha\ (\text{rad}), p\ (\text{rad/s}), q\ (\text{rad/s}), r\ (\text{rad/s}), \phi\ (\text{rad/s}), \theta\ (\text{rad/s}), \psi\ (\text{rad/s})]$ and $u := [\delta_{\text{ail}}\ (\text{rad}),\ \delta_{\text{ele}}\ (\text{rad}), \delta_{\text{rud}}\ (\text{rad}), T\ (\text{N})]$. The body axis and stability axis system used can be seen in Figure 2.

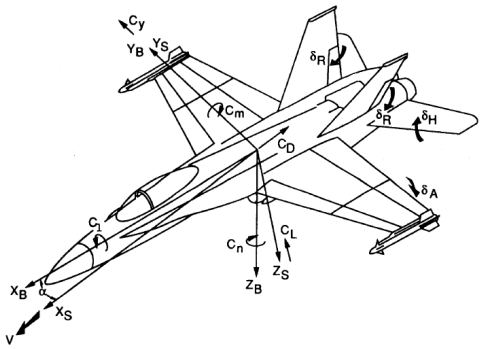

Fig. 2 Body axis and stability axis system with control surface sign conventions. [21]

Figure 2 shows an F/A-18 aircraft flying in steady level flight at an angle of attack α, which can be seen in the difference in the body axes (denoted by a subscript B) and the stability axes (denoted by a subscript S). The roll, pitch, and yaw moment coefficients (C_l, C_m, and C_n) are defined about body frame axes X_B, Y_B, and Z_B respectively. The lift, drag, and side force coefficients (C_L, C_D, and C_Y) are defined as positive along $-Z_S$, $-X_S$, and $+Y_S$ respectively. The Euler angles ϕ, θ, and ψ are rotations of the body axes, whereas the angles α and β are aerodynamic angles defined relative to the direction the aircraft is moving within the airflow V. The rate of change of the rotation of the aircraft's body axes is related to the roll, pitch, and yaw rates (p, q, r) as follows:

$$\begin{bmatrix} \dot{\phi} \\ \dot{\theta} \\ \dot{\psi} \end{bmatrix} = \begin{bmatrix} 1 & \sin\phi\tan\theta & \cos\phi\tan\theta \\ 0 & \cos\phi & -\sin\phi \\ 0 & \sin\phi\sec\theta & \cos\phi\sec\theta \end{bmatrix} \begin{bmatrix} p \\ q \\ r \end{bmatrix} \tag{18}$$

The force equations are given as follows:

$$\begin{aligned} \dot{V} = &-\frac{\bar{q}S}{m}C_{D_{\text{wind}}} + g(\cos\phi\cos\theta\sin\alpha\cos\beta + \sin\phi\cos\theta\sin\beta) \\ &- g(\sin\theta\cos\alpha\cos\beta) + \frac{T}{m}\cos\alpha\cos\beta \end{aligned} \tag{19}$$

$$\begin{aligned} \dot{\alpha} = &-\frac{\bar{q}S}{mV\cos\beta}C_L + q - \tan\beta(p\cos\alpha + r\sin\alpha) \\ &+ \frac{g}{V\cos\beta}(\cos\phi\cos\theta\cos\alpha + \sin\theta\sin\alpha) - \frac{T\sin\alpha}{mV\cos\beta} \end{aligned} \tag{20}$$

$$\begin{aligned} \dot{\beta} = &\frac{\bar{q}S}{mV}C_{Y_{\text{wind}}} + p\sin\alpha - r\cos\alpha + \frac{g}{V}\cos\beta\sin\phi\cos\theta \\ &+ \frac{\sin\beta}{V}(g\cos\alpha\sin\theta - g\sin\alpha\cos\phi\cos\theta + \frac{T}{m}\cos\alpha) \end{aligned} \tag{21}$$

where

$$C_{D_{\text{wind}}} = C_D\cos\beta - C_Y\sin\beta \tag{22}$$

$$C_{Y_{\text{wind}}} = C_Y \cos\beta + C_D \sin\beta \tag{23}$$

Finally, the rate of change of the roll, pitch, and yaw rates are related to the rates themselves and the roll, pitch, and yaw moment coefficients as follows:

$$\dot{p} = \frac{1}{\kappa}\left(\left[(\bar{q}Sb)(I_{zz}C_l + I_{xz}C_n)\right] - \left[I_{xz}^2 + I_{zz}(I_{zz} - I_{yy})\right]qr\right) \tag{24}$$

$$\dot{q} = \frac{1}{I_{yy}}\left(\bar{q}S\bar{c}C_m + (I_{zz} - I_{xx})pr\right) \tag{25}$$

$$\dot{r} = \frac{1}{\kappa}\left(\left[(\bar{q}Sb)(I_{xz}C_l + I_{xx}C_n)\right] + \left[I_{xz}^2 + I_{xx}(I_{xx} - I_{yy})\right]pq\right) \tag{26}$$

where $\kappa = I_{xx}I_{zz} - I_{xz}^2$.

2.6 Controller Model

Figure 3 shows the simplified control law used to examine closed-loop dynamic behaviour. This controller structure is based on the Control Augmentation System (CAS) presented in Buttrill et al[21].

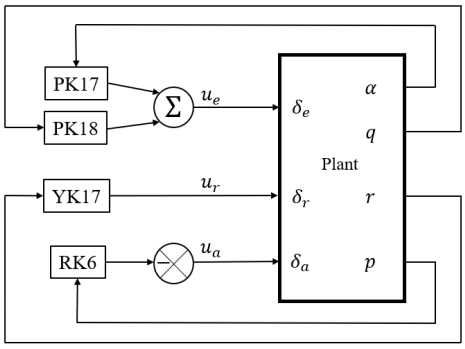

Fig. 3 Flight Control Law

For the sake of simplicity, actuator dynamics and several filters are ignored and the controller only uses feedback of α, q, r, and p. In longitudinal feedback, the angle of attack α and pitch rate q have the gains defined by Buttrill as PK17 and PK18 respectively. The rudder channel feedback is multiplied by the gain given in function YK17. The roll channel feedback is multiplied by gain given by function RK6 and multiplied again by a factor of -1. Nominal refuelling conditions given in Table 3 correspond to gains of PK17 = 0.5, PK18 = 0.47, YK17 = 0.84, and RK6 = 0.169. Thrust is assumed to be held constant at its trim value in all analyses. This gives the plant measurements y into the controller as $y := [V\ \beta\ \alpha\ p\ q\ r\ \phi\ \theta\ \psi]$ and the controller input vector as $u := [\delta_{\text{ail}}\ \delta_{\text{ele}}\ \delta_{\text{rud}}]$. The baseline controller feedback matrix can be seen in Equation 27.

$$\left[K\right] = \begin{bmatrix} 0 & 0 & 0 & RK6 & 0 & 0 & 0 & 0 & 0 \\ 0 & 0 & -PK17 & 0 & -PK18 & 0 & 0 & 0 & 0 \\ 0 & 0 & 0 & 0 & 0 & -YK17 & 0 & 0 & 0 \end{bmatrix} \tag{27}$$

3 Validation

This section presents validation of the tanker wake velocities produced by the vortex panel/actuator disk model of a C-130 Hercules, and the open-loop dynamic modes of an F/A-18 aircraft. Additionally, the closed-loop dynamic modes of the F/A-18 are also examined to confirm that the addition of the controller model leads to improvements in handling qualities.

3.1 Wake Model

Vicroy *et al.*[22] published flight test data in which a C-130 Hercules weighing approximately 45000 kg, and flying at a altitude of 5000 ft. and a speed of Mach 0.28 was used as a wake generator. The induced wake velocity was measured by a OV-10 aircraft flying approximately 450 m behind the C-130 aircraft. The vortex panel representation of the Hercules aircraft used will be identical to the dimensions published by Bloy and Trochadilis[5]. The centre of gravity (CG) of the C-130 was assumed to be aligned with the centre line approximately 0.7 m aft of the wing's leading edge.

A comparison of the C-130 Hercules wake measured during flight tests, and the wake generated by a vortex panel method can be seen in Figure 4.

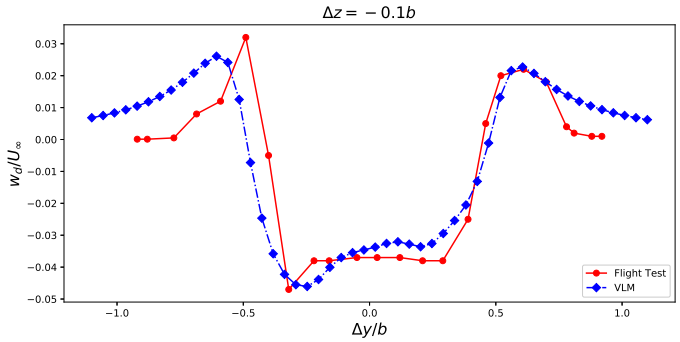

Fig. 4 Downwash profile of a C-130 Hercules flying at 5000 ft, Ma = 0.28

The downwash profiles show good agreement with each other in terms of both upwash and downwash magnitude and location of the maximum wake velocities. The addition of the propulsion model appears to also capture the asymmetry present in the flight test data. It can be seen that the upwash values outboard of the wing at $\pm 0.5\Delta y/b$ do not decay with lateral offset as rapidly in the vortex panel data compared to the flight test data. This is likely caused by viscous effects, such as vortex decay, that are not accounted for in the vortex panel method. As the wake measurements were conducted approximately 450 m behind the C-130 during the flight test, it is expected that some vortex decay would be seen in this area of the farfield.

3.2 Controller and Dynamic Model

In order to validate the aerodynamic and dynamic model, the eigenvalues of the aircraft's dynamic modes published in NASA Technical Publication TP-1998-208465 (High-Alpha Research Vehicle Lateral-Directional Control Law Description, Analyses, and Simulation Results)[23] and NASA Technical Paper 3446 (High-Alpha Research Vehicle Longitudinal Controller: Design, Analyses, and Simulation Results)[24] were used as a basis for comparison. NASA's High-Alpha Research Vehicle (HARV) was a modified F/A-18 which was developed to study high angle of attack technologies including thrust-vectoring and other advanced aerodynamic controls.

Table 1 Trim Conditions and Open-Loop Short-Period Frequencies

Flight Conditions		Published[24]		Model	
Altitude (ft.)	Mach (-)	Trim α (deg.)	Short-Period Freq. (rad/s)	Trim α (deg.)	Short-Period Freq. (rad/s)
15,000	0.70	2.52	2.7	2.66	2.39
15,000	0.49	5.0	1.4	5.8	1.4
25,000	0.70	3.58	2.1	3.47	1.9
25,000	0.59	5.0	1.5	5.36	1.4
35,000	0.70	5.34	1.5	4.85	1.5
35,000	0.60	7.24	1.0	7.43	1.1

Table 2 Trim Conditions and Open-Loop Lateral-Directional Eigenvalues

	Published[23]				Model			
Mach (-)	Trim α (deg.)	Spiral	Roll	Dutch Roll	Trim α (deg.)	Spiral	Roll	Dutch Roll
0.59	5.0	0.004	-1.40	-0.20$\pm$1.67i	5.36	-0.03	-1.00	-0.41$\pm$1.50i
0.41	10.0	0.011	-0.74	-0.21$\pm$1.58i	11.6	-0.06	-0.46	-0.34$\pm$1.52i
0.36	15.0	0.006	-0.46	-0.19$\pm$1.56i	15.6	-0.08	-0.35	-0.27$\pm$1.54i
0.33	20.0	-0.033	-0.28	-0.16$\pm$1.77i	18.1	-0.09	-0.30	-0.23$\pm$1.55i

The model shows a slight tendency to under-predict the short-period frequency at higher mach numbers. However, because most AAR takes place below M=0.6, this is not considered a serious problem. The lateral-directional modes show good agreement in terms of Dutch roll frequency and roll subsistence, although the predicted Dutch roll damping is higher than the published values. Additionally, the published data indicates an unstable spiral mode for the F/A-18 which the model does not. In practice, the unstable spiral mode necessitates the use of a washout filter, as per Buttrill et al[21]. In order to evaluate the controller model and gains, the predicted handling qualities of both the open-loop and closed-loop systems were examined for the flight conditions given in Tables 1 and 2. The comparison of the handling qualities based on the short period can be seen below in Figure 5.

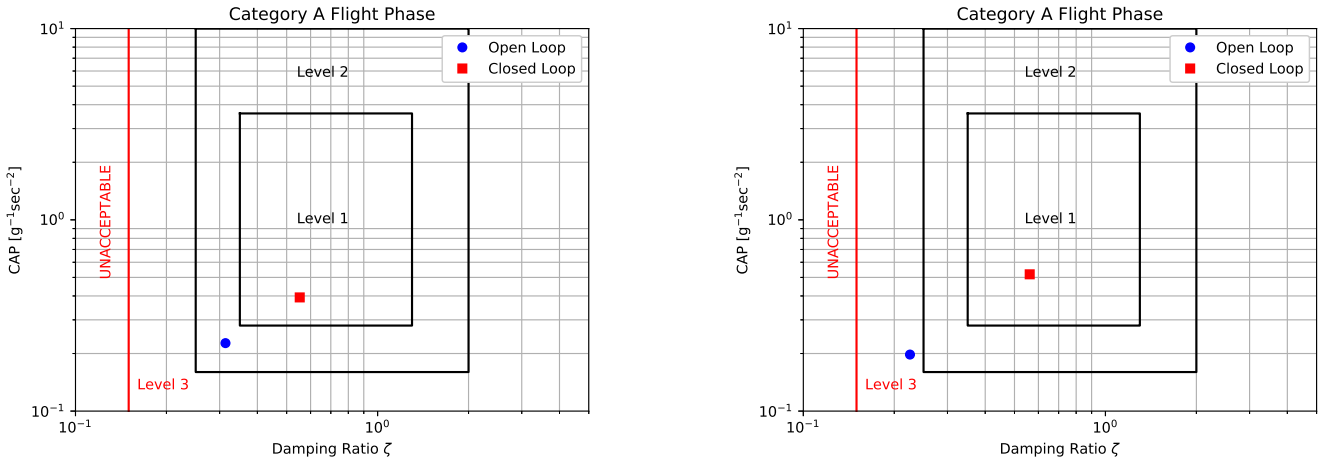

(a) 15,000 ft., M=0.7 **(b) 35,000 ft., M=0.6**

Fig. 5 Comparison of open-loop and closed-loop flying qualities based on the short period at two flight conditions.

The CAP relates initial pitching acceleration to steady-state normal acceleration and is defined as $\frac{\omega_n^2}{n/\alpha}$ where n/α is

$$\frac{n}{\alpha} = \frac{U_\infty}{g}\left[\frac{-M_\alpha Z_\delta + Z_\alpha M_\delta}{-M_q Z_\delta + M_\delta q}\right] \tag{28}$$

where $Z_\delta = \frac{-QS}{m}\frac{\partial C_L}{\partial \delta_e}$ and $M_\delta = \frac{QSc}{I_{yy}}\frac{\partial C_m}{\partial \delta_e}$. Figure 5 shows a clear improvement in the handling qualities between the open-loop and closed-loop plant across different flight conditions. At the higher speed, lower altitude flight condition, the open-loop system is predicted to have Level 2 handling qualities, and at the lower speed, higher altitude flight condition, the open-loop system is predicted to have Level 3 handling qualities. In both cases, the short period damping and the CAP are too small to allow for Level 1 handling qualities. At both flight conditions, the addition of the α and pitch rate p feedback increases damping and CAP and improves the handling qualities to Level 1. This shows that the addition of the controller in the closed-loop system functions as expected.

When examining the Dutch roll and lateral-directional handling qualities, the addition of a washout filter was also examined. The comparison of the flying qualities based on the Dutch roll can be seen below in Figure 6.

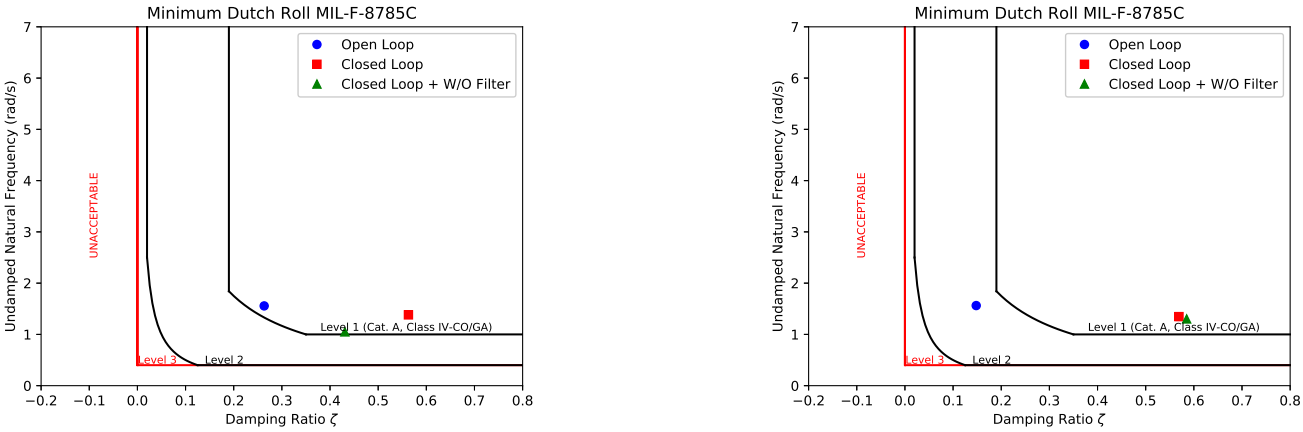

(a) 25,000 ft., M=0.59 **(b) 25,000 ft., M=0.33**

Fig. 6 Comparison of open-loop and closed-loop flying qualities based on the Dutch roll at two flight conditions.

It can be seen that the closed loop system has little effect on the natural frequency of the Dutch roll while increasing the damping, as we would expect in a well-designed controller system. Additionally, it can be seen that the use of a washout filter at higher mach can result in both a reduction in damping and frequency compared to the simple closed loop model. For this reason, in addition to the lack of an unstable spiral mode, it was decided to not include the washout filter in the closed loop analysis.

4 Results and Discussion

The tanker/refueller pair chosen for the analysis in this work was a C-130 tanker with a F/A-18 refueller. These aircraft were chosen due to the relatively large amount of public data available on both aircraft, and because they are a tanker/refueller combination that is still in use in the Royal Canadian Air Force (RCAF). Analyses were performed assuming the nominal refuelling conditions shown in Table 3. All

analyses were performed with a 5m longitudinal separation between the tail of the C-130 and the nose of the F/A-18. The typical vortex panel representation of this flight formation can be seen in Figure 7.

Table 3 Refuelling Conditions

Parameter	Value	Units
Airspeed	250	KIAS
Altitude	20,000	ft.
ρ_∞	0.653	kg/m^3
a	316	m/s
M_∞	0.54	-

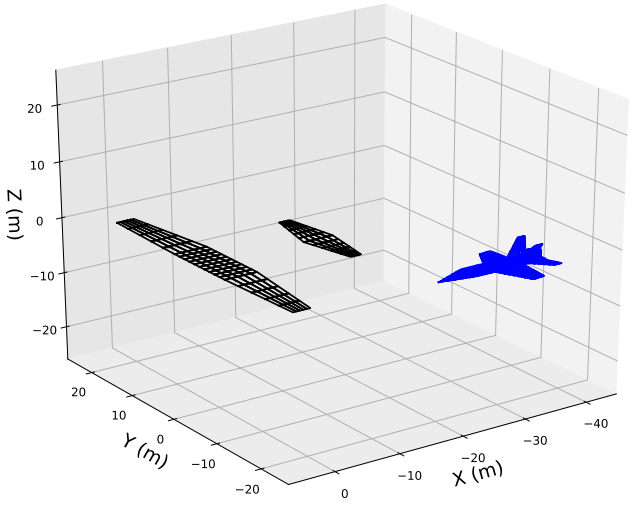

Fig. 7 Vortex panel representation of the C-130 (black) and F/A-18 (blue) flying in close formation.

Figure 8 shows the pitch, roll, and aileron and rudder deflections required to achieve trim with the F/A-18's centre of gravity at various points in the wake of the C-130 The figures also show an outline of the C-130's wing and propeller location to aid in interpretability.

In general, the deleterious effects of flying within the propwash can be seen as there are rapid changes in the flight angles and control surface deflections required to maintain trim. Even outside of the direct propwash, asymmetrical effects due to the propellers can be seen, as larger pitch angles, roll angles, and control surface deflections are required to maintain trim when flying close to the left wingtip compared to when flying close to the right wingtip.

By finding trim points at different locations in the wake, the positional stability can be examined in terms of control surface deflections, rather than change in induced moments. This is done by evaluating the changes in wake velocities with respect to Y and Z at each trim point and using the trim equations to predict the required change in control surface deflections to counteract these changes. The aircraft is said to be positionally stable if forces in the wake tend to return the refuelling aircraft back to its original position when disturbed[7]. Required change in control surface deflection with respect to change in lateral position can be seen in Figure 9.

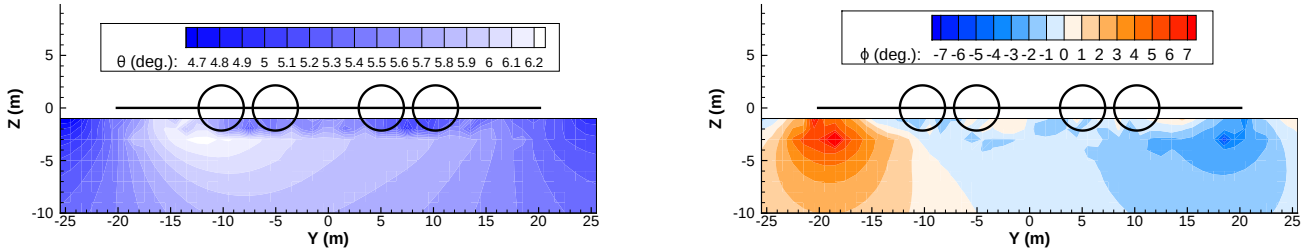

(a) Pitch Angle θ

(b) Roll Angle ϕ

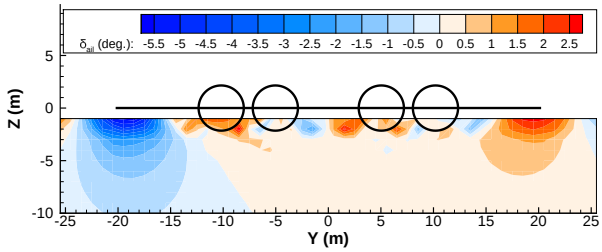

(c) Aileron deflection δ_{ail}

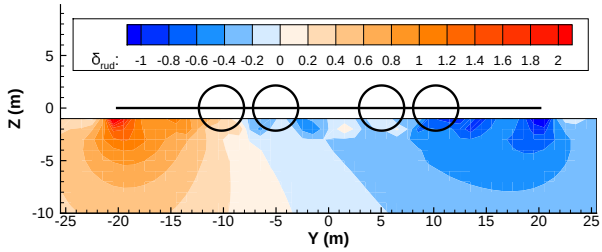

(d) Rudder deflection δ_{rud}

Fig. 8 Trim pitch and roll angles with control surface deflections at various points in the wake behind a C-130 at 20,000 ft, M=0.54. Longitudinal separation = 5 m.

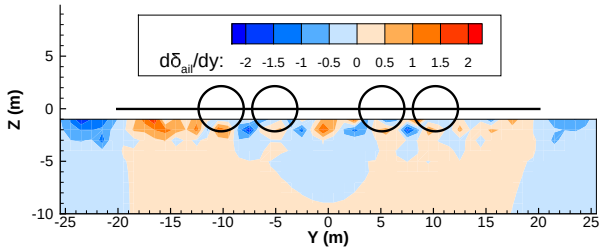

(a) Aileron deflection stability

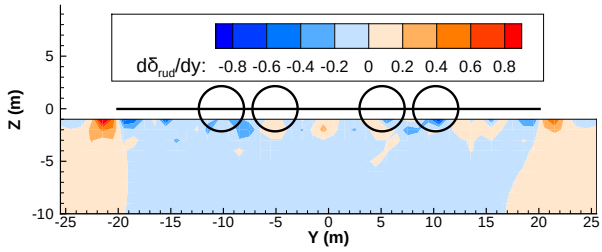

(b) Rudder deflection stability

Fig. 9 Change in control surface deflection at trim with respect to change in lateral position at various points in the wake behind a C-130 at 20,000 ft, M=0.54. Longitudinal separation = 5 m.

At most locations immediately behind the C-130's wing, the aileron deflection stability is positive. This means that as the F/A-18 moves in the positive Y direction, an increase in positive (right) aileron is required to maintain trim. Without this, the refuelling aircraft will tend back towards its initial position, indicating positional stability in the roll axis. Similarly, at these same locations negative rudder deflection stability can be seen. Based on the sign convention used here, left rudder is positive. As the F/A-18 moves in the positive Y direction, an increase in negative (right) rudder is required to maintain trim. Without this, the refuelling aircraft will begin to yaw to the left, back towards its initial position, indicating positional stability in the yaw axis. These areas of positional stability are roughly analogous to those shown by Blake and Gingras[7].

The flying qualities based on MIL-HDBK-1797 and MIL-F-8785C are typically based on the natural frequencies and damping of the dynamic modes. When flying within the wake, the closed-loop analysis does not predict a large change in eigenvalues compared to free steady level flight, as the aerodynamic stiffness and damping do not change appreciably. However, while the eigenvalues themselves may not undergo large changes, the addition of an effective sideslip angle β and bank angle ϕ at trim leads to cross-coupling of the dynamic modes. A phasor plot of the 9-state dynamic modes for the F/A-18 trimmed the location of maximum roll angle at trim with $\theta = 5.72^o$ and $\phi = 6.66^o$ can be seen in Figure 10. The phasor plots are colour coded such that eigenvector components associated with rotations about the x axis, are shown in orange, eigenvector components associated with rotations about the y axis are shown in purple, and eigenvector components associated with rotations about the z axis are shown in

blue.

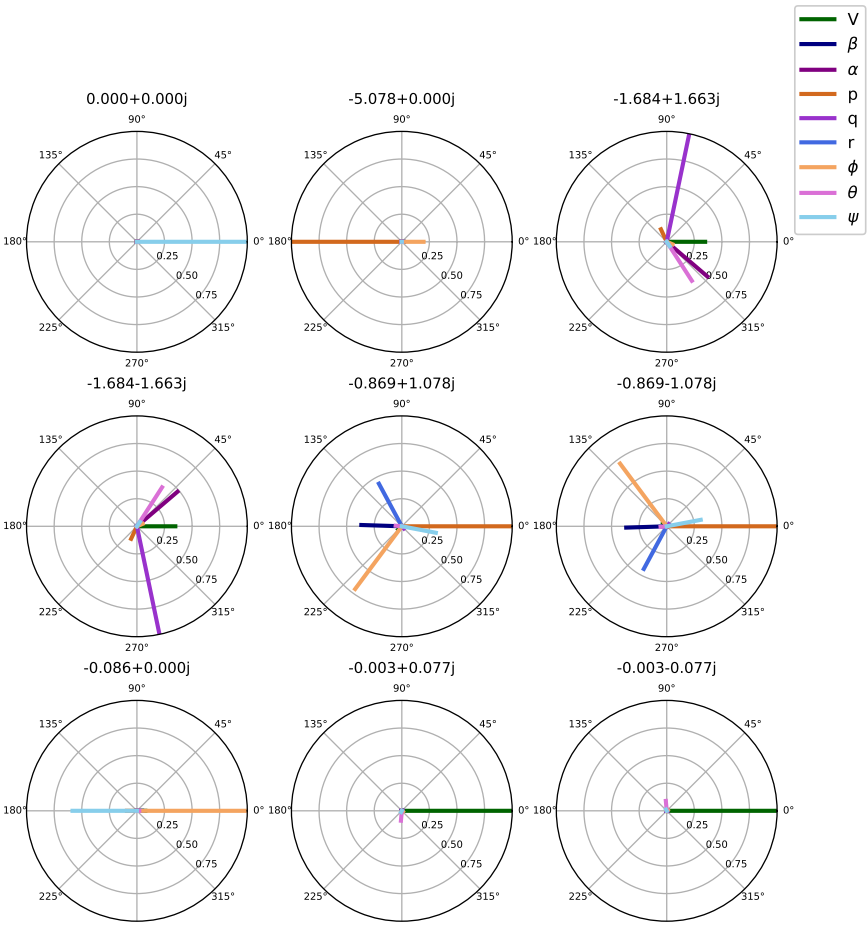

Fig. 10 Phasor plot of the dynamic modes of an F/A-18 trimmed at $\theta = 5.72^o$ and $\phi = 6.66^o$

The cross-coupling of the dynamic modes is most clearly seen in the short period, whose eigenvalue is $1.684 \pm 1.663\,j$. While the short period is normally considered a longitudinal mode, components of p, ϕ, and ψ can also be seen. Additionally, there are small longitudinal components present in the eigenvectors of the Dutch roll mode. Given that changes in position within the wake result in changes to the trim condition, it stands to reason that the introduction of cross-coupling will result in undesirable handling qualities regardless of the flying qualities given from a purely frequency based analysis, particularly in circumstances of moderate atmospheric turbulence. Therefore, it is the position of the authors that the flying qualities given in MIL-HDBK-1797 and MIL-F-8785C should be re-examined for AAR-based refuelling tasks.

5 Conclusion

This paper demonstrated the use of a multi-modal analysis framework designed to rapidly analyze tanker/refueller interactions during AAR. In addition to calculating trim points within the tanker wake and identifying the regions of positional stability and instability, a major goal in the development of this framework is to predict handling qualities in order to make quantitative and qualitative predictions about pilot workload during the AAR task. While the closed-loop eigenvalues can be found, the cross-coupling which appears in the eigenvectors, together with changes to the trim state with changes in position, makes it unlikely that a purely frequency-based approach to handling quality prediction will be adequate. Therefore, future work will examine frequency-based handling quality prediction, as seen in Iloputaife et al.[25] and Lu et al.[12], and further work will involve explicitly time-stepped simulations designed to examine perturbation responses in the time-domain.

Appendix

The appendix contains the details of the aerodynamic model used in this paper based on the model published by Chakraborty et al.[18]

$$\begin{aligned} C_m =& \left(C_{m\alpha 3}\alpha^3 + C_{m\alpha 2}\alpha^2 + C_{m\alpha 1}\alpha\right) + \left(C_{m\delta_e 2}\alpha^2 + C_{m\delta_e 1}\alpha + C_{m\delta_e 0}\right)\delta_e \\ &+ \frac{\bar{c}}{2V}\left(C_{mq3}\alpha^3 + C_{mq2}\alpha^2 + C_{mq1}\alpha + C_{mq0}\right)q \end{aligned} \tag{29}$$

Table 4 Pitching Moment Coefficient Model Data

Airframe	Control Surfaces	Rates
$C_{m\alpha 3} = -1.5022$	$C_{m\delta_e 2} = 0.9338$	$C_{mq3} = 64.7190$
$C_{m\alpha 2} = 0.9176$	$C_{m\delta_e 1} = -0.3245$	$C_{mq2} = -68.5641$
$C_{m\alpha 1} = -0.3823$	$C_{m\delta_e 0} = -0.9051$	$C_{mq1} = 10.9921$
		$C_{mq0} = -4.1186$

$$\begin{aligned} C_l =& \left(C_{l\beta 4}\alpha^4 + C_{l\beta 3}\alpha^3 + C_{l\beta 2}\alpha^2 + C_{l\beta 1}\alpha + C_{l\beta 0}\right)\beta \\ &+ \left(C_{l\delta_a 3}\alpha^3 + C_{l\delta_a 2}\alpha^2 + C_{l\delta_a 1}\alpha + C_{l\delta_a 0}\right)\delta_a \\ &+ \left(C_{l\delta_r 3}\alpha^3 + C_{l\delta_r 2}\alpha^2 + C_{l\delta_r 1}\alpha + C_{l\delta_r 0}\right)\delta_r \\ &+ \frac{b}{2V}\left(C_{lp1}\alpha + C_{lp0}\right)p + \frac{b}{2V}\left(C_{lr2}\alpha^2 + C_{lr1}\alpha + C_{lr0}\right)r \end{aligned} \tag{30}$$

Table 5 Rolling Moment Coefficient Model Data

Airframe	Control Surfaces	Rates
$C_{l\beta 4} = -1.6196$	$C_{l\delta_a 3} = 0.1989$	$C_{lp1} = 0.2377$
$C_{l\beta 3} = 2.3843$	$C_{l\delta_a 2} = -0.2646$	$C_{lp0} = -0.3540$
$C_{l\beta 2} = -0.3620$	$C_{l\delta_a 1} = -0.0516$	$C_{lr2} = -1.0871$
$C_{l\beta 1} = -0.4153$	$C_{l\delta_a 0} = 0.1424$	$C_{lr1} = 0.7804$
$C_{l\beta 0} = -0.0556$	$C_{l\delta_r 3} = -0.0274$	$C_{lr0} = 0.1983$
	$C_{l\delta_r 2} = 0.0083$	
	$C_{l\delta_r 1} = 0.0014$	
	$C_{l\delta_r 0} = 0.0129$	

$$\begin{aligned} C_n =& \left(C_{n\beta 2}\alpha^2 + C_{n\beta 1}\alpha + C_{n\beta 0}\right)\beta \\ &+ \left(C_{n\delta_a 3}\alpha^3 + C_{n\delta_a 2}\alpha^2 + C_{n\delta_a 1}\alpha + C_{n\delta_a 0}\right)\delta_a \\ &+ \left(C_{n\delta_r 4}\alpha^4 + C_{n\delta_r 3}\alpha^3 + C_{n\delta_r 2}\alpha^2 + C_{n\delta_r 1}\alpha + C_{n\delta_r 0}\right)\delta_r \\ &+ \frac{b}{2V}\left(C_{np1}\alpha + C_{np0}\right)p + \frac{b}{2V}\left(C_{nr1}\alpha + C_{nr0}\right)r \end{aligned} \tag{31}$$

Table 6 Yawing Moment Coefficient Model Data

Airframe	Control Surfaces	Rates
$C_{n\beta 2} = -0.3816$	$C_{n\delta_a 3} = 0.2694$	$C_{np1} = -0.0881$
$C_{n\beta 1} = 0.0329$	$C_{n\delta_a 2} = -0.3413$	$C_{np0} = 0.0792$
$C_{n\beta 0} = 0.0885$	$C_{n\delta_a 1} = 0.0584$	$C_{nr1} = -0.1307$
	$C_{n\delta_a 0} = 0.0104$	$C_{nr0} = -0.4326$
	$C_{n\delta_r 4} = 0.3899$	
	$C_{n\delta_r 3} = -0.8980$	
	$C_{n\delta_r 2} = 0.5564$	
	$C_{n\delta_r 1} = -0.0176$	
	$C_{n\delta_r 0} = -0.0780$	

$$\begin{aligned} C_Y =& \left(C_{Y\beta 2}\alpha^2 + C_{Y\beta 1}\alpha + C_{Y\beta 0}\right)\beta \\ &+ \left(C_{Y\delta_a 3}\alpha^3 + C_{Y\delta_a 2}\alpha^2 + C_{Y\delta_a 1}\alpha + C_{Y\delta_a 0}\right)\delta_a \\ &+ \left(C_{Y\delta_r 3}\alpha^3 + C_{Y\delta_r 2}\alpha^2 + C_{Y\delta_r 1}\alpha + C_{Y\delta_r 0}\right)\delta_r \end{aligned} \tag{32}$$

Table 7 Pitching Moment Coefficient Model Data

Airframe	Control Surfaces
$C_{Y\beta 2} = -0.1926$	$C_{Y\delta_a 3} = -0.8500$
$C_{Y\beta 1} = 0.2654$	$C_{Y\delta_a 2} = 1.5317$
$C_{Y\beta 0} = -0.7344$	$C_{Y\delta_a 1} = 0.2403$
	$C_{Y\delta_a 0} = -0.1656$
	$C_{Y\delta_r 3} = 0.9351$
	$C_{Y\delta_r 2} = -1.6921$
	$C_{Y\delta_r 1} = 0.4082$
	$C_{Y\delta_r 0} = 0.2054$

$$\begin{aligned} C_D =& \left(C_{D\alpha 4}\alpha^4 + C_{D\alpha 3}\alpha^3 + C_{D\alpha 2}\alpha^2 + C_{D\alpha 1}\alpha + C_{D\alpha 0}\right)\cos\beta + C_{D_0} \\ &+ \left(C_{D\delta_e 3}\alpha^3 + C_{D\delta_e 2}\alpha^2 + C_{D\delta_e 1}\alpha + C_{D\delta_e 0}\right)\delta_e \end{aligned} \tag{33}$$

Table 8 Lift Coefficient Model Data

Airframe	Control Surfaces
$C_{D\alpha 4} = 1.4610$	$C_{L\delta_e 3} = -3.8578$
$C_{D\alpha 3} = -5.7341$	$C_{L\delta_e 2} = 4.2360$
$C_{D\alpha 2} = 6.3971$	$C_{L\delta_e 1} = -0.2739$
$C_{D\alpha 1} = -0.1995$	$C_{L\delta_e 0} = 0.0366$
$C_{D\alpha 0} = -1.4994$	
$C_{D_0} = 1.5036$	

Acknowledgements

The authors wish to acknowledge and thank the Directorate of Technical Airworthiness and Engineering Support (DTAES) at Canada's Department of National Defence (DND) for supporting this research (Grant #18485SK101-07).

References

[1] NATO. *Guide to Obtaining Air-to-Air Refuelling Clearances and Compatibility Certification*. North Atlantic Treaty Organization, February 2016.

[2] P.R. Thomas, U. Bhandari, S. Bullock, T.S. Richardson, and J.L. duBois. Advances in air-to-air refueling. *Progress In Aerospace Science*, 71:pp. 14–35, 2014.

[3] W. Mao and F.O. Eke. A survey of the dynamics and control of aircraft during aerial refueling. *Nonlinear Dynamics and Systems Theory*, 8(4):pp. 375–388, 2008.

[4] AW Bloy, PJ Lamont, HA Abu-Assaf, and KAM Ali. The lateral dynamic stability and control of a large receiver aircraft during air-to-air refuelling. *Aeronautical Journal*, 90:237–243, 1986.

[5] AW Bloy and V Trochalidis. The performance and longitudinal stability and control of large receiver aircraft during air to air refuelling. *Aeronautical Journal*, 93(930):367–378, 1989.

[6] W.B. Blake. An aerodynamic model for simulation of close formation flight. In *AIAA Modeling and Simulation Technologies Conference and Exhibit*, number AIAA 2000-4304, Denver, CO, August 2000. Air Force Research Laboratory, AIAA.

[7] W.B. Blake and D.R. Gingras. Comparison of predicted and measured formation flight interference effects. *Journal of Aircraft*, 41(2):pp. 201–207, March–April 2004.

[8] Atilla Dogan, William Blake, and Christian Haag. Bow wave effect in aerial refueling: Computational analysis and modeling. *Journal of Aircraft*, 50(6):1856–1868, 2013.

[9] Atilla Dogan and William Blake. Modeling of bow wave effect in aerial refueling. In *AIAA Atmospheric Flight Mechanics Conference*, page 7926, 2010.

[10] A. Dogan, S. Sato, and W.B. Blake. Flight control and simulation for aerial refueling. In *AIAA Guidance, Navigation, and Control Conference and Exhibit*, number AIAA 2005-6264, San Francisco, CA, August 2005. AIAA.

[11] Nicolas Fezans and Thomas Jann. Modeling and simulation for the automation of aerial refueling of military transport aircraft with the probe-and-drogue system. In *AIAA Modeling and Simulation Technologies Conference*, page 4008, 2017.

[12] Chang Lu, Lixin Wang, Ting Yue, and Hailiang Liu. Longitudinal flying qualities evaluation method for receiver in probe and drogue aerial refueling. In *2020 11th International Conference on Mechanical and Aerospace Engineering (ICMAE)*, pages 87–92. IEEE, 2020.

[13] Luke H Peristy, Ruben E Perez, and Peter W Jansen. Flying qualities prediction tool for aerial refuelling operational compatibility assessment. In *AIAA Scitech 2020 Forum*, page 1261, 2020.

[14] Joseph Katz and Allen Plotkin. *Low-speed aerodynamics*, volume 13. Cambridge University Press, 2001.

[15] John T Conway. Analytical solutions for the actuator disk with variable radial distribution of load. *Journal of Fluid Mechanics*, 297:327–355, 1995.

[16] Giovanni Droandi and Giuseppe Gibertini. Assessment of a propeller model embedded on a panel method code for aircraft aerodynamics. *The Journal of Aerospace Science, Technology and Systems*, 91(3/4):98–108, 2012.

[17] Christian Alba, Ali Elham, Brian German, and Leo L Veldhuis. A surrogate-based multi-disciplinary design optimization framework exploiting wing-propeller interaction. In *18th AIAA/ISSMO Multidisciplinary Analysis and Optimization Conference*, page 4329, 2017.

[18] Abhijit Chakraborty. Linear and nonlinear analysis of susceptibility of F/A-18 flight control laws to the falling leaf mode. Master's thesis, 2010.

[19] Marcello R. Napolitano and Joelle M. Spagnuolo. Determination of the stability and control derivatives of the NASA F/A-18 HARV using flight data. Technical report, NASA, 1993.

[20] Kenneth W Iliff and Kon-Sheng Charles Wang. Extraction of lateral-directional stability and control derivatives for the basic F-18 aircraft at high angles of attack. Technical report, NASA, 1997.

[21] Carey S. Buttrill, P. Douglas Arbuckle, and Keith D. Hoffler. Simulation model of a twin-tail, high performance airplane. Technical report, NASA, 1992.

[22] Dan D Vicroy, Paul M Vijgen, Heidi M Reimer, Joey L Gallegos, and Philippe R Spalart. Recent nasa wake-vortex flight tests, flow-physics database and wake-development analysis. In *1998 World Aviation Conference*, volume 107, pages 1764–1777. AMERICAN TECHNICAL PUBLISHERS LTD, 1998.

[23] John B Davidson. *High-alpha research vehicle lateral-directional control law description, analyses, and simulation results*. National Aeronautics and Space Administration, Langley Research Center, 1998.

[24] Aaron J Ostroff, Keith D Hoffler, and Melissa S Proffitt. *High-Alpha Research Vehicle (HARV) Longitudinal Controller: Design, Analyses, and Simulation Results*. National Aeronautics and Space Administration, Langley Research Center, 1994.

[25] Obi Iloputaife, Gerald Svoboda, and T Bailey. Handling qualities design of the c-17a for receiver-refueling. In *Guidance, Navigation, and Control Conference*, page 3746, 1996.